Interfacial Energetics Reversal Strategy for Efficient Perovskite Solar Cells

Sheng Jiang[1,9], Shaobing Xiong[1,9], Zhongcheng Yuan[2,9], Yafang Li[1], Xiaomeng You[3], Hongbo Wu[4], Menghui Jia[5], Zhennan Lin[1], Zaifei Ma[4], Yuning Wu[1], Yefeng Yao[3], Xianjie Liu[6], Junhao Chu[7], Zhenrong Sun[5], Mats Fahlman[6]*, Henry J. Snaith[2]*, Qinye Bao[1,8]*

[1]*School of Physics and Electronic Science, East China Normal University, Shanghai, China*

[2]*Clarendon Laboratory, Department of Physics, University of Oxford, Oxford, UK*

[3]*Shanghai Key Laboratory of Magnetic Resonance, East China Normal University, Shanghai, China*

[4]*Center for Advanced Low-Dimension Materials, Donghua University, Shanghai, China*

[5]*State Key Laboratory of Precision Spectroscopy, East China Normal University, Shanghai, China*

[6]*Laboratory of Organic Electronics, Linköping University, Norrköping, Sweden*

[7]*Shanghai Frontiers Science Research Base of Intelligent Optoelectronics and Perception, Institute of Optoelectronics, Fudan University, Shanghai, China*

[8]*Collaborative Innovation Center of Extreme Optics, Shanxi University, Taiyuan, China*

[9]*These authors contributed equally: Sheng Jiang, Shaobing Xiong, Zhongcheng Yuan*

*Corresponding authors.

E-mail: mats.fahlman@liu.se (F. M.); henry.snaith@physics.ox.ac.uk (H. J. S.); qybao@clpm.ecnu.edu.cn (Q. B.)

Abstract

Reducing heterointerface nonradiative recombination is a key challenge for realizing highly efficient perovskite solar cells (PSCs). Motivated by this, we develop a facile strategy *via* interfacial energetics reversal to functionalize perovskite heterointerface. A surfactant molecule, trichloro[3-(pentafluorophenyl)propyl]silane (TPFS) reverses perovskite surface energetics from intrinsic n-type to p-type, evidently demonstrated by ultraviolet and inverse photoelectron spectroscopies. The reconstructed perovskite surface energetics match well with upper deposited hole transport layer, realizing an exquisite energy level alignment for accelerating hole extraction across the heterointerface. Meanwhile, TPFS further diminishes surface defect density. As a result, this cooperative strategy leads to greatly minimized nonradiative recombination. PSCs achieve an impressive power conversion efficiency of 25.9% with excellent reproducibility, and a nonradiative recombination induced qV_{oc} loss of only 57 meV, which is the smallest reported to date in n-i-p structured PSCs.

Introduction

Metal halide perovskite solar cells (PSCs) have aroused widespread interests in both academia and industry as a promising next-generation photovoltaic technology, due to their exceptionally high-power conversion efficiency (PCE), low cost and great application potential[1]. The perovskite semiconductors as sunlight absorber possess various impressive optoelectronic properties, including high absorption coefficients[2,3], small exciton binding energies[4,5], long carrier diffusion lengths[6,7] and tunable band gaps[8,9]. The certified PCE of single-junction PSC hence is approaching that of silicon solar cells recently[10-12]. Nevertheless, nonradiative recombination happening at the heterointerfaces between perovskite film and charge transport layer significantly influences the performance of PSCs, causing a large gap between actual device output efficiency and thermodynamic limit[13-15].

Commonly, solution-processed perovskite films are in polycrystalline state with abundant intrinsic defects on the crystal surface, causing nonradiative recombination of photogenerated carrier at the heterointerfaces[16-18]. Surface defect-passivators effectively reduces trap-assisted nonradiative recombination[19-21], resulting in especially improved open-circuit photovoltage (V_{oc}) and operational stability. Another important source for nonradiative recombination is energetics mismatch at the heterointerfaces between perovskite film and charge transport layer[22,23], though being of vital importance and determining device photovoltaic parameters, *i.e.,* V_{oc} and fill factor (FF), which has been overlooked. For example, in a *n-i-p* (*p-i-n*) structured PSC, a perovskite film deposited on cathode (anode) substrates with low (high) work function (WF) preferentially presents a more n- (p-) type surface energetic due to self-doping, however, which leads to detrimental electrical contact with sequentially upper p-type hole transport layer, HTL (n-type electron transport layer, ETL)[24,25]. Such unmatched contact impedes hole (electron) extraction efficacy across the heterointerface from perovskite to HTL (ETL) and causes serious interfacial nonradiative recombination in PSCs[26-28]. Therefore, it is an extreme need for exploring efficient strategies to mediate this

energetics mismatch at the perovskite heterointerface and dramatically suppress nonradiative recombination in the PSCs, which remains an ongoing challenge.

Herein, we develop a facile interfacial energetics reversal strategy to reduce nonradiative recombination and achieve high performance PSCs. Multiple characterizations reveal that a surfactant molecule, Trichloro[3-(pentafluorophenyl)propyl]silane (TPFS) reverses perovskite surface energetics from intrinsic n-type to p-type, and the reconstructed perovskite surface energetics accelerate hole extraction across the heterointerface from perovskite to HTL. Meanwhile, TPFS passivates defects and suppresses leakage current. As a result, the TPFS-treated PSCs achieve an efficiency of 25.9% and a nonradiative recombination induced qV_{oc} loss of only 57 meV, the smallest reported to date in *n-i-p* structured devices, to the best of our knowledge. The treated devices exhibit greatly enhanced reproducibility and stability, retaining ~ 95% of its initial efficiency under MPP tracking for 900 h at 50±5 ℃.

Results and Discussion

Energetics reversal mechanism

Fig. 1a illustrates heterointerface reconstruction process of a $FAPbI_3$ perovskite film deposited on stannic oxide (SnO_2), where a very thin TPFS is spin-coated on the surface of the $FAPbI_3$ perovskite film followed by a thermal annealing process. We carry out ultraviolet and inverse photoelectron spectroscopies (UPS and IPES) to investigate the surface energetics of perovskite films (**Fig. 1b-1c)**. The control perovskite film grown on cathode SnO_2 has an intrinsic low WF of 4.25 eV and an ionization potential (IP) of 5.55 eV. After modifying the perovskite surface with TPFS molecules, we observe a large 600 meV increase in WF of the perovskite film (from 4.25 to 4.85 eV) due to the electronegativity of fluorine (F) and thus electron transfer from perovskite to F **(Supplementary Fig. 1)**, while the IP remains constant at 5.55 eV. Considering the IP of TPFS is 8.2 eV and UPS is an extremely surface-sensitive technology with the probing depth of around 1 nm, observing identical IP and UPS spectral features in the

control and TPFS-treated perovskite mean that TPFS molecules diffuse into the perovskite surface region along the crystal grain boundaries during thermal annealing process. This also agrees well with our theoretical calculation results shown in **Fig. 1a**. The perovskite valance band maximum (VBM) position with respect to Fermi level (E_F) is determined at the intersection of the UPS valence spectrum onset on a logarithmic scale, and the conductive band minimum (CBM) position with respect to E_F is determined by an extrapolation of the IPES spectrum edge on a linear scale, respectively. We find that the electron affinity (EA) of both the control and TPFS-treated perovskite films are 4.02 eV, and their charge transport band gaps are 1.53 eV, which further prove that TPFS does not form a layer on top of the perovskite.

Fig. 1d-1e shows corresponding energy level diagrams derived from UPS and IPES combinations for the control and TPFS-treated perovskite films. Clearly, the E_F with respect to VBM shifts from 1.30 to 0.70 eV, implying that the surface energetics of the TPFS-treated perovskite film completely reverse from intrinsic n-type to p-type. The reconstructed perovskite surface p-type energetics match better with the upper p-type HTL and promote hole extraction across the heterointerface from perovskite to HTL, which therefore prevents nonradiative recombination induced by carrier accumulation.

We utilize Kelvin probe force microscopy (KPFM) to examine the surface morphology and potential distribution of perovskite films. The TPFS-treated perovskite film exhibits an improved contact potential relative to the control **(Fig. 2a-2b)**, in accordance with the UPS results. The TPFS-treated perovskite film shows a slightly lower surface roughness (**Supplementary Fig. 2**), which is believed to be beneficial for forming a better contact with the upper HTL[29]. X-ray photoelectron spectroscopy (XPS) Pb 4f and I 3d core levels shift to lower binding energies by 0.6 eV in the TPFS-treated perovskite film **(Fig. 2c** and **Supplementary Fig. 3)**, indicative of a shift in the E_F toward VBM, and further validating the UPS and IPES with the reversal direction from intrinsic n-type to p-type on perovskite surface. This reversal is confirmed by a Hall coefficient (R_H) from a negative -1.26 m^3 C^{-1} to a positive 1.01 m^3 C^{-1} **(Fig. 2d)**. In addition, the

penetrating depth of the TPFS molecules into the perovskite films is estimated to be around 100 nm *via* cross-sectional KPFM potential profiles **(Supplementary Fig. 4)**. The *in-situ* formed n-p homojunction **Fig. 2e**) from bulk to surface region in the perovskite film enhances built-in electric field in the PSCs **(Supplementary Fig. 5)**.

We study the interaction between perovskite compositions and TPFS by ^{1}H nuclear magnetic resonance (NMR) and ^{19}F NMR. The resonance signal of the N-H splits into two new peaks respectively at 8.73 and 8.99 ppm with the addition of TPFS **(Fig. 2f)**, while the ^{19}F protons from TPFS exhibit an obvious chemical shift by 0.1 ppm **(Fig. 2g)**. These results suggest the formation of hydrogen bond (N-H···F) between the FA cations and the TPFS molecules [30], which can be further confirmed by an obvious shift of N-H stretching (*v* N-H) peak from 3402 to 3410 cm^{-1} **(Supplementary Fig. 6)** in the Fourier transform infrared (FTIR) spectra. The hydrogen bonds immobilize FA cations in the grain surface area and stabilize perovskite crystal structures[31]. Furthermore, we observe Si-Cl stretching (*v* Si-Cl) peak in the TPFS-treated perovskite shifts toward higher wavenumber **(Supplementary Fig. 7)**, while the ^{207}Pb NMR spectra shows a lower chemical shift **(Fig. 2h)**. Moreover, the XPS Cl 2p core level spectra shift to higher binding energies (**Supplementary Fig. 8)**, which is also in contrast with the shift of Pb 4f core level spectra to lower binding energies **(Fig. 2c)**. The results above consolidate the atomic-Cl of TPFS passivation on surface Pb^{2+} defects by forming Pb-Cl coordinate bonds[32]. The theoretical model of the interaction between perovskite and TPFS is calculated and summarized in **Fig. 2i**.

Carrier dynamics

To gain profound insight into the pivotal role in carrier dynamics by TPFS at perovskite heterointerface, we conduct photoluminescence (PL) spectroscopy and ultrafast transient absorption spectroscopy (UTAS) tests. The TPFS-treated perovskite film presents enhancements both in steady-state PL intensity **(Fig. 3a)** and time-resolved PL (TRPL) lifetime **(Supplementary Fig. 12 and Supplementary Table 1)**. We further notice that the defect density decreases from 2.16×10^{15} to 1.13×10^{15} cm^{-3} as obtained

from space charge-limited current (SCLC) curves (using pulsed voltage scanning to avoid impact from ions migration, details in Methods)[33] **(Fig. 3b)**. These results above provide compelling evidence of diminished defects in the TPFS-treated perovskite film. When the TPFS-treated perovskite contacts with Spiro-OMeTAD HTL, we further observe a faster TRPL decay with an average carrier lifetime from 5.59 to 3.06 ns **(Fig. 3c)**. We compare their UTAS and the TPFS-treated perovskite with HTL shows a faster ground-state bleaching (GSB) recovery compared to the control **(Fig. 3d-3e** and **Supplementary Fig. 13)**. Tracking the respective GSB decays at 780 nm, more efficient hole extraction is achieved after TPFS modification (**Fig. 3f**), demonstrating the enhanced hole extraction at the perovskite/HTL heterointerface[34]. We conclude that the TPFS helps to boost hole extraction across the contact from perovskite to HTL due to energetics reversal. The improved charge transport at the heterointerface effectively suppresses nonradiative recombination, which is highly favorable for obtaining higher V_{oc} and FF in PSCs[12].

Photovoltaic performance

We fabricate a planar PSC with normal configuration of ITO/SnO_2/perovskite/TPFS/Spiro-OMeTAD/MoO_x/Ag **(Supplementary Fig. 14)**. The concentration of TPFS is optimized to be 5 mg mL^{-1} in isopropyl alcohol (IPA) **(Supplementary Fig. 15, 16** and **Supplementary Table 2)**. **Fig. 4a** shows the current density-voltage (*J-V*) plots of the PSCs under AM 1.5G simulated solar illumination. The control device shows a typical PCE of 22.5%, with a moderate V_{oc} of 1.117 V, a short-circuit current (J_{sc}) of 25.49 mA cm^{-2} and an FF of 79.14%. In contrast, the TPFS-treated device exhibits a remarkably improved PCE of 25.9%, with a higher V_{oc} of 1.185 V, J_{sc} of 25.72 mA cm^{-2}, FF of 84.84% and negligible hysteresis behavior **(Supplementary Fig. 17** and **Supplementary Table 3)**. As mentioned above, we believe that the improved device performance is ascribed to the enhanced charge extraction efficacy at the hole-selective contact.

We observe similar integrated J_{sc} values to those from the *J-V* curves according to

external quantum efficiency (EQE) spectra **(Fig. 4b)**. The statistical analysis of the photovoltaic parameters based on 25 cells for each type shows a better reproducibility **(Fig. 4c, d** and **Supplementary Fig. 18)**. The TPFS-treated device obtains a stable photocurrent density and PCE of 24.56 mA cm^{-2} and 25.5% respectively at the maximum power point (MPP) tracking for 300 s **(Fig. 4e)**. To understand the enhanced V_{oc} of the TPFS treated perovskite devices, we carry out capacitance-voltage (*C-V*) plots to extract the built-in potential (V_{bi}) according to the Mott-Schottky equation[35]: $\frac{1}{C^2} = \frac{2(V_{bi}-V)}{A^2 e\varepsilon\varepsilon_0 N_A}$, where A is device area, ε_0 is vacuum permittivity, ε is relative permittivity[36], and N_A is carrier concentration. The V_{bi} increases from 0.90 (control) to 1.00 V (TPFS-treated) due to the energetics reversal that facilities charge transport in PSCs **(Fig. 4f)**. Moreover, the transient photovoltage (TPV) decay under V_{oc} presents a longer carrier lifetime of 6.56 μs than 4.96 μs **(Supplementary Fig. 19)**, in accordance with the increased recombination resistance (R_{rec}) in the electrical impedance spectroscopy **(Supplementary Fig. 20 and Supplementary Table 4)**.

We further study the effect of TPFS on the stability of the unencapsulated devices. The TPFS-treated device retains over 90% of its initial efficiency after 2000 h under 60±5% RH in ambient condition, whereas the control device losses ~40% of its initial efficiency **(Fig. 4g)**. The TPFS-treated device maintains ~ 95% of its initial efficiency during maximum power point (MPP) tracking for 900 h at 50±5 °C in N_2 condition **(**T_{95} ≈ 900 h**, Fig. 4h)**. We believe the enhanced stability is attributed to the hydrogen bonding and the defect passivating between perovskite compositions and TPFS, and the improved energetics alignment at the TPFS-treated perovskite hole-selective heterointerface, as well as an enhanced hydrophobicity of the TPFS-treated perovskite film inferred from the increased water contact angle **(Supplementary Fig. 21)**. In addition, the upshifted vacuum level with respect to E_F accompanied by the enhanced WF **(Fig. 1d, e)** also improves the activation energy of halogen migration across the heterointerface and increases the device lifetime[37].

To explore the nonradiative recombination mechanisms of the TPFS-treated PSCs, we characterize the leakage current from the dark *J-V* curves **(Supplementary Fig. 22)**. We observe lower leakage current at negative bias of the TPFS-treated device, indicating a suppressed nonradiative recombination. We perform light intensity (P) dependent V_{oc} and J_{sc} of the devices, respectively. According to the equation[38]: $V_{oc} = \frac{nkTln(P)}{q}$, where n is ideality factor, k is Boltzmann constant, T is absolute temperature, and q is elementary charge, the TPFS-treated device shows a smaller slope of 1.42 in term of kT/q than the 1.67 slope of the control **(Fig. 5a)**, revealing that TPFS effectively reduces the trap-assisted nonradiative recombination. The exponential factor α deduced from the express $J_{sc} \propto P^{\alpha}$ increases in the TPFS-treated device **(Supplementary Fig. 23)**, suggesting a suppressed interfacial nonradiative recombination.

We conduct analyses of open-circuit photovoltage loss and FF loss of the TPFS-treated PSCs. **Fig. 5b** displays the external quantum efficiencies of electroluminescence (EQE_{EL}) *versus* injection current density curves of PSC when operating as light-emitting diodes (LEDs). We obtain EQE_{EL} values of 0.96% and 11.10% at the current density close to the J_{sc} of the control and TPFS-treated devices. As per the detailed balance theory[39]: $\Delta V_{oc,\ nonrad} = -\frac{kT}{q}\ln(EQE_{EL})$, they show 120 and 57 meV of the nonradiative recombination induced qV_{oc} loss ($\Delta qV_{oc,\ nonrad}$) of control and TPFS-treated devices, respectively (**Supplementary Note 1**). To the best of our knowledge, this $\Delta qV_{oc,\ nonrad}$ of the TPFS-treated device is the lowest value reported to date in *n-i-p* structured PSCs **(Fig. 5c** and **Supplementary Table 5)**, demonstrating the excellent impact of TPFS on reducing nonradiative recombination. By contrast, the slight improvement of 2 meV in the radiative recombination loss ($\Delta qV_{oc,\ rad}$) is secondary, as revealed by the high-sensitivity EQE near the band edge (**Supplementary Fig. 24**). It is thus clear that the suppressed nonradiative recombination is the main factor contributing to the increased V_{oc} of the TPFS-treated devices **(Fig. 5d)**.

The maximum FF (FF_{max}) without charge transport loss is estimated by the equation[40]: $FF_{max} = \frac{V_A - \ln(V_A + 0.72)}{V_A + 1}$, where $V_A = \frac{qV_{oc}}{nk_BT}$. The discrepancy of FF_{max} is consistent with the suppression of nonradiative recombination loss in PSCs. The charge transport induced FF loss declines from 6.28% to 1.91%, because of the increased hole extraction efficiency at the perovskite/HTL heterointerface originating from energetics reversal (**Fig. 5e**).

Conclusion

In summary, we have demonstrated a facile interfacial energetics reversal strategy to reduce nonradiative recombination for high-efficiency PSCs. The TPFS molecule reverses the perovskite surface energetics from the intrinsic n-type perovskite film to p-type, leading to well matched energy level with the upper HTL for accelerated hole extraction at the heterointerface. Meanwhile, the incorporation of TFPS reduces perovskite films surface defects. As a result, the TPFS-treated PSCs achieve a remarkable efficiency of 25.9%, and a smallest nonradiative recombination induced qV_{oc} loss of 57 meV reported to date in *n-i-p* PSCs. Our work develops a promising strategy from the energetical view to modulate perovskite heterointerface for improving the efficiency and stability of PSCs.

Materials and Methods

Materials

Formamidinium iodide (FAI) and methylamine hydrochloride (MACl) was purchased from Greatcell Solar Ltd. Lead iodide (PbI_2) and 2,2',7,7'-Tetrakis(N,N-di-p-methoxyphenylamino)-9,9'-spirobifluorene (Spiro-OMeTAD) were received from Advanced Election Technology Co. Ltd. Bis(trifluoromethanesulfonyl)imide lithium (Li-TFSI) and tertbutyl pyridine (tBP) were purchased from Xi'an Polymer Light Technology Corp. Stannic oxide (SnO_2) colloid dispersion and rubidium chloride (RbCl) were obtained from Alfa-Aesar. Trichloro[3-(pentafluorophenyl)propyl]silane (TPFS) and molybdenum trioxide (MoO_3) were purchased from TCI. All materials were used

as received without any further purification.

PSC fabrication and characterization

The pre-patterned ITO glasses were cleaned with detergent, deionized water, acetone, ethanol, and isopropanol in sequence under ultrasonication for each 20 min, and then treated with UV-ozone for 20 min. The SnO_2 colloid precursor was diluted using ultrapure water (1:6 in volume ratio) and spin-coated on the ITO substrates at 3000 rpm for 30 s, and then annealed on a hotplate at 150 ℃ for 30 min. 1.5 M PbI_2 doped with 5% RbCl in DMF: DMSO (9:1) solvent was spin-coated onto SnO_2 at 1500 rpm for 30 s, and annealed at 70 °C for 1 min, then cooled to room temperature. A solution of FAI: MACl (90 mg: 15 mg in 1 ml IPA) was spin-coated onto the PbI_2 film at 1800 rpm for 30 s in N_2-filled glove box, and then the films were annealed at ambient condition at 150 °C for 15 min (at 35% relative humidity). The TPFS was dissolved in IPA with the different concentrations and was spin-coated on the prepared perovskite films at 4000 rpm for 30 s, followed by a thermal annealing process at 100 ℃ for 5 min. The thickness of the TPFS is estimated to be ~8 nm. The upper hole transport layer Spiro-OMeTAD (72.3 mg Spiro-OMeTAD in CB with 28.8 μL tBP and 17.5 μL Li-TFSI solution with 520 mg mL^{-1} in acetonitrile) was deposited on the perovskite film via spin-coating at 4000 rpm for 30 s. After storage in dry air overnight, 5 nm MoO_3 and 100 nm Ag were thermally evaporated with a mask at a pressure of 10^{-5} mbar.

The current-voltage (*J-V*) curves of solar cells were measured under Enli solar simulator (SSF5-3A, Enlitech) via a Keithley 2400 series source meter in N_2-filled glovebox without any preconditioning, and the light intensity was calibrated by a NREL-certified standard Si solar cell with KG-5 filter (SRC-2020, Enlitech). The device active area is 0.05 cm^2 determined by the aperture shade mask to avoid overestimation of the photocurrent density. The external quantum efficiency (EQE) was recorded by a QE-R system. The capacitance-voltage (*C-V*) curve was conducted by an impedance spectroscope (PGSTAT302N, Autolab) at the frequency of 50 KHz. The electrical impedance spectroscopy (EIS) measurement was performed via a precision

impedance analyzer (IM6ex, Zahner, Germany). Transient photovoltage (TPV) decay was obtained by a digital oscilloscope (DOS-X3104A) at open-circuit condition. The operational stability of the unencapsulated devices at the MPP tracking was tested in nitrogen atmosphere. The illumination was provided by a commercial xenon lamp with light intensity calibrated to one sun (AM 1.5G) by a NREL certified Si cell, and the device temperature during MPP was monitored by an infrared thermometer. The hole-only devices were prepared with a structure of ITO/PTAA/perovskite/TPFS/Spiro-OMeTAD/Ag and the J-V curves were obtained by scanning the devices with pulsed voltages under dark condition to avoid the influence of mobile ions. The scanning time interval between two adjacent voltage points was set for 5s.

Film characterization

X-ray diffraction (XRD) patterns were recorded by PANalytical X-ray diffractometer with Cu Kα radiation. UV-vis absorption spectra were collected from a UV-vis-NIR spectrometer (TU-1901). Atomic force microscope (AFM) was used to determine film thickness of TPFS. Fourier-transform infrared (FTIR) measurements were performed by a PerkinElmer FTIR spectrometer with an attenuated total reflectance accessory. Steady-state PL spectra were recorded by a fluorescence spectrometer (PerkinElmer LS 55) using a 465 nm excitation light source, and the time-resolved PL decay was recorded via a time-corrected single photo counting system at an excitation wavelength of 373 nm. Liquid-state ^{1}H and ^{19}F Nuclear magnetic resonance (NMR) spectra were acquired at room temperature using a Bruker Avance HD X500 500MHz spectrometer. The delay time was set to 30 s to allow for complete relaxation. Solid-state NMR spectra were acquired at room temperature using a Bruker Avance III 600 MHz NMR spectrometer equipped with a 4 mm cross polarization-magic-angle spinning (CP-MAS) probe. The solid-state ^{207}Pb NMR spectra were acquired using a single-pulse excitation pulse sequence. The spinning rate was set to 10 kHz, and the recycle delay was 2 s. Hall effect measurement was characterized by Nanometrics HL5500 Hall System with 4-probe device structures. A magnetic field (B) (0-0.5 T) perpendicular to the sample surface was applied, and the Hall voltage (V_H) across the sample was recorded with

Keithley Model 4200 when a direct current (I, 5 mA) was applied using Keithley Model 2400.

Ultraviolet and X-ray photoelectron spectroscopy

Ultraviolet and X-ray photoelectron spectroscopy (UPS and XPS) measurements were carried out in an ultrahigh vacuum surface analysis system equipped with a Scienta-R3000 spectrometer. UPS employed a monochromatic He I light (21.22 eV) as excitation source with an energy resolution of 50 meV. The work function and valence band maximum were derived from the secondary electron cutoff and the frontier edge of the occupied density states to vacuum level, respectively. XPS was measured using the monochromatic Al Kα (1486.6 eV) as excitation source. All spectra were calibrated by referring to the Fermi level and Au $4f_{7/2}$ position of the Ar^+ ion sputter-cleaned Au foil, and Fermi level was referred as the zero-binding energy.

Inverse photoelectron spectroscopy

Inverse photoelectron spectroscopy (IPES) measurement was carried out in an ultrahigh vacuum surface analysis system using the isochromatic mode, with electron energies from -9.9 to -3 eV onto the sample. The conductive band minimum edge and the electron affinity were determined in IPES.

Ultrafast transient absorption spectroscopy

Ultrafast transient absorption spectroscopy (UTAS) was carried out by a Ti: Sapphire laser system (Coherent, Astrella), which provides 800 nm fundamental pulse with pulse width of 35 fs at 1 kHz. The fundamental pulses were separated to two light beams, where the pump beam (515 nm) was generated by an optical parametric amplifier (OPerA Solo, Coherent Inc.), and the probe beam (white light continuum) was generated by focusing on a sapphire slice. The pump and probe beams were spatially overlapped on the sample at a small angle less than 10°. The transmitted probe light from sample was collected by a linear charge coupled device (CCD) array.

Electroluminescence efficiency measurement

The electroluminescence (EL) spectra were recorded by a kymerra-3281 spectrograph and a Si EMCCD camera (DU970PBVF, Andor). EL external quantum efficiency (EQE_{EL}) was performed via a digital source meter (Keithley 2400) for driving the solar cells with different voltages and a picometer (Keithley 6482) with a calibrated Si photodiode for quantifying photon flux from the device. The solar cells working area were encapsulated and the measurements were performed in ambient environment.

Highly sensitive external quantum efficiency measurement

Sensitive external quantum efficiency (EQE) spectra were measured by using monochromatic light from a halogen lamp light source (LSH-75, Newport) and a monochromator (CS260-RG-3-MC-A, Newport). A series of long-pass optical filters (600, 900 and 1100 nm) were employed to eliminate the overtone wavelengths from the monochromator. The monochromatic light was chopped at a frequency of 173 Hz by an optical chopper (3502 Optical Chopper, Newport). A frontend current amplifier (SR570, Stanford Instrument) and a phase-locked amplifier (SR830, Stanford Instrument) were used to record the current signal from the solar cells. A Si detector (Hamamatsu s1337-1010BR) was used to calibrate the lamp intensity.

Density functional theory calculation

To evaluate whether the TPFS molecules stayed in perovskites, the model was built where TPFS was located between two $FAPbI_3$ layers with a gap of about 8 Å. The structure was fully relaxed until the total force on each atom was lower than 0.01 eV $Å^{-1}$, by the density functional theory (DFT) as implemented in the plane-wave-based Quantum-Espresso (QE) package. The Perdew-Burke-Ernzerhof (PBE) exchange-correction functional was selected, and the projector augmented-wave (PAW) pseudopotential with an energy cutoff of 550 eV was employed, and a single Γ point was adopted. Bader charge analysis was applied to estimate the charge transfer between perovskite and molecule.

Supporting Information

Supporting Information is available.

Acknowledgements

The work is supported by the National Natural Science Foundation of China grant (62322407, 22279034, 52261145698, W2421103), the National Key Research and Development Program of China (2022YFB3803300), Shanghai Science and Technology Innovation Action Plan (22ZR1418900, 24110714100), and East China Normal University Multifunctional Platform for Innovation. This work was also funded by the Engineering and Physical Science Research Council (EPSRC, grant EP/X038777/1), UK. M. F. acknowledges the support from the STINT grant (CH2017-7163) and the Swedish Government Strategic Research Area in Materials Science on Functional Materials at Linköping University (Faculty Grant SFO Mat LiU no. 2009 00971). Z.Y. acknowledges the support from Marie Skłodowska Curie Actions Postdoc Fellow (UKRI Guarantee, grant numbers EP/Y029135/1).

Author contributions

Q.B. H.J.S and M.F. supervised the research project. S.J., S.X. and Z.Y. fabricated the devices, conducted the characterizations, and wrote the manuscript. S.J. and S.X. performed the UPS, IPES and XPS measurements. Y.L. contributed to the AFM and KPFM measurements. X.Y. and Y.Y. carried out the NMR measurements. H.W. performed the EQE_{EL} measurements and Z.Y. analyzed the V_{oc} loss. M.J. conducted the UTAS and TRPL measurements. Z.L. and Y.W. performed the DFT calculations. X.L., J.C., Z.S., M.F., H.J.S and Q.B. contributed to the data analysis and revised the manuscript. All authors discussed the results and contributed to the manuscript.

Conflict of Interest

H.J.S is co-founder and Chief Scientific Officer of Oxford PV Ltd. All other authors declare no competing interests.

References

1. Duan, T. et al. Chiral-structured heterointerfaces enable durable perovskite solar cells. *Science* **384**, 878-884 (2024).
2. Kojima, A., Teshima, K., Shirai, Y. & Miyasaka, T. Organometal halide perovskites as visible-light sensitizers for photovoltaic cells. *J. Am. Chem. Soc.* **131**, 6050-6051 (2009).
3. Burschka, J. et al. Sequential deposition as a route to high-performance perovskite-sensitized solar cells. *Nature* **499**, 316-319 (2013).
4. Brenner, T., Egger, D., Kronik, L., Hodes, G. & Cahen, D. Hybrid organic-inorganic perovskites: low-cost semiconductors with intriguing charge-transport properties. *Nat. Rev. Mater.* **1**, 15007 (2016).
5. Lee, M., Teuscher, J., Miyasaka, T., Murakami, T. N. & Snaith, H. J. Efficient hybrid solar cells based on meso-superstructured organometal halide perovskites. *Science* **338**, 643-647 (2012).
6. Pazos-Outon, L. M. et al. Photon recycling in lead iodide perovskite solar cells. *Science* **351**, 1430-1433 (2016).
7. Stranks, S. D. et al. Electron-hole diffusion lengths exceeding 1 micrometer in an organometal trihalide perovskite absorber. *Science* **342**, 341-344 (2013).
8. Filip, M. R., Eperon, G. E., Snaith, H. J. & Giustino, F. Steric engineering of metal-halide perovskites with tunable optical band gaps. *Nat. Commun.* **5**, 5757 (2014).
9. Zhang, W., Eperon, G. E. & Snaith, H. J. Metal halide perovskites for energy applications. *Nat. Energy* **1**, 16048 (2016).
10. Zhou, J. et al. Highly efficient and stable perovskite solar cells via a multifunctional hole transporting material. *Joule* **8**, 1-16 (2024).
11. Sidhik, S. et al. Two-dimensional perovskite templates for durable, efficient formamidinium perovskite solar cells. *Science* **384**, 1227-1235 (2024).
12. Chen, H. et al. Improved charge extraction in inverted perovskite solar cells with dual-site-binding ligands. *Science* **384**, 189-193 (2024).
13. Warby, J. et al. Understanding performance limiting interfacial recombination in perovskite solar cells. *Adv. Energy Mater.* **12**, 2103567 (2022).
14. Wolff, C. M., Caprioglio, P., Stolterfoht, M. & Neher, D. Nonradiative recombination in perovskite solar cells: the role of interfaces. *Adv. Mater.* **31**, 1902762 (2019).
15. Luo, D., Su, R., Zhang, W., Gong, Q. & Zhu, R. Minimizing non-radiative recombination losses in perovskite solar cells. *Nat. Rev. Mater.* **5**, 44-60 (2020).
16. Yang, J. et al. Energetics and energy loss in 2D ruddlesden-popper perovskite solar cells. *Adv. Energy Mater.* **10**, 2000687 (2020).
17. Schulz, P., Cahen, D. & Kahn, A. Halide perovskites: is it all about the interfaces? *Chem. Rev.* **119**, 3349-3417 (2019).
18. Zheng, Y. et al. Towards 26% efficiency in inverted perovskite solar cells interfacial flipped band bending and suppressed deep-level traps. *Energy*

Environ. Sci. **17**, 1153-1162 (2024).
19. Jiang, Q. et al. Surface passivation of perovskite film for efficient solar cells. *Nat. Photonics* **13**, 460-466 (2019).
20. Xu, Y. et al. Synchronous modulation of defects and buried Interfaces for highly efficient inverted perovskite solar cells. *Adv. Energy Mater.* **13**, 2203505 (2023).
21. Zang, X. et al. Passivating dipole layer bridged 3D/2D perovskite heterojunction for highly efficient and stable p-i-n solar cells. *Adv. Mater.* **36**, 2309991 (2024).
22. Noel, N. K. et al. Interfacial charge-transfer doping of metal halide perovskites for high performance photovoltaics. *Energy Environ. Sci.* **12**, 3063-3073 (2019).
23. Xiong, S. et al. Reducing nonradiative recombination for highly efficient inverted perovskite solar cells via a synergistic bimolecular interface. *Nat. Commun.* **15**, 5607 (2024).
24. Olthof, S. & Meerholz, K. Substrate-dependent electronic structure and film formation of $MAPbI_3$ perovskites. *Sci. Rep.* **7**, 40267 (2017).
25. Miller, E. M. et al. Substrate-controlled band positions in $CH_3NH_3Pbl_3$ perovskite films. *Phys. Chem. Chem. Phys.* **16**, 22122-22130 (2014).
26. Xiong, S. et al. Surface charge-transfer doping for highly efficient perovskite solar cells. *Nano Energy* **79**, 105505 (2021).
27. Euvrard, J., Yan, Y. & Mitzi, D. B. Electrical doping in halide perovskites. *Nat. Rev. Mater.* **6**, 531-549 (2021).
28. Jiang, S. et al. In situ reconstruction of hole-selective perovskite heterojunction with graded energetics toward highly efficient and stable solar cells. *Adv. Energy Mater.* **13**, 2300983 (2023).
29. Jiang, S. et al. Constructing chromium multioxide hole-selective heterojunction for high-performance perovskite solar cells. *Adv. Sci.* **9**, 2203681 (2022).
30. Yuan, S. et al. NbF: a novel a-phase stabilizer for FA-based perovskite solar cells with high efficiency. *Adv. Func. Mater.* **29**, 1807850 (2019).
31. Li, M. et al. Orientated crystallization of FA-based perovskite via hydrogen-bonded polymer network for efficient and stable solar cells. *Nat. Commun.* **14**, 573 (2023).
32. Wu, J. et al. Regioselective multisite atomic-chlorine passivation enables efficient and stable perovskite solar cells. *J. Am. Chem. Soc.* **145**, 5872-5879 (2023).
33. Duijnstee, E. A. et al. Toward understanding space-charge limited current measurements on metal halide perovskites. *ACS Energy Lett* **5**, 376-384 (2020).
34. Wu, T. et al. Enhancing the hot carrier injection of perovskite solar cells by incorporating a molecular dipole interlayer. *Adv. Func. Mater.* **32**, 2204450 (2022).
35. Almora, O., Aranda, C., Mas-Marza, E. & Garcia-Belmonte, G. On mott-schottky analysis interpretation of capacitance measurements in organometal perovskite solar cells. *Appl. Phys. Lett.* **109**, 173903 (2016).
36. Park, J. et al. Controlled growth of perovskite layers with volatile alkylammonium chlorides. *Nature* **616**, 724-730 (2023).

37. Tan, S. et al. Stability-limiting heterointerfaces of perovskite photovoltaics. *Nature* **605**, 268-273 (2022).
38. Fu, S. et al. Efficient passivation with lead pyridine-2-carboxylic for high-performance and stable perovskite solar cells. *Adv. Energy Mater.* **9**, 1901852 (2019).
39. Lu, H. et al. Vapor-assisted deposition of highly efficient, stable black-phase $FAPbI_3$ perovskite solar cells. *Science* **370**, eabb8985 (2020).
40. Jeong, M. J. et al. Boosting radiation of stacked halide layer for perovskite solar cells with efficiency over 25%. *Joule* **7**, 112-127 (2023).

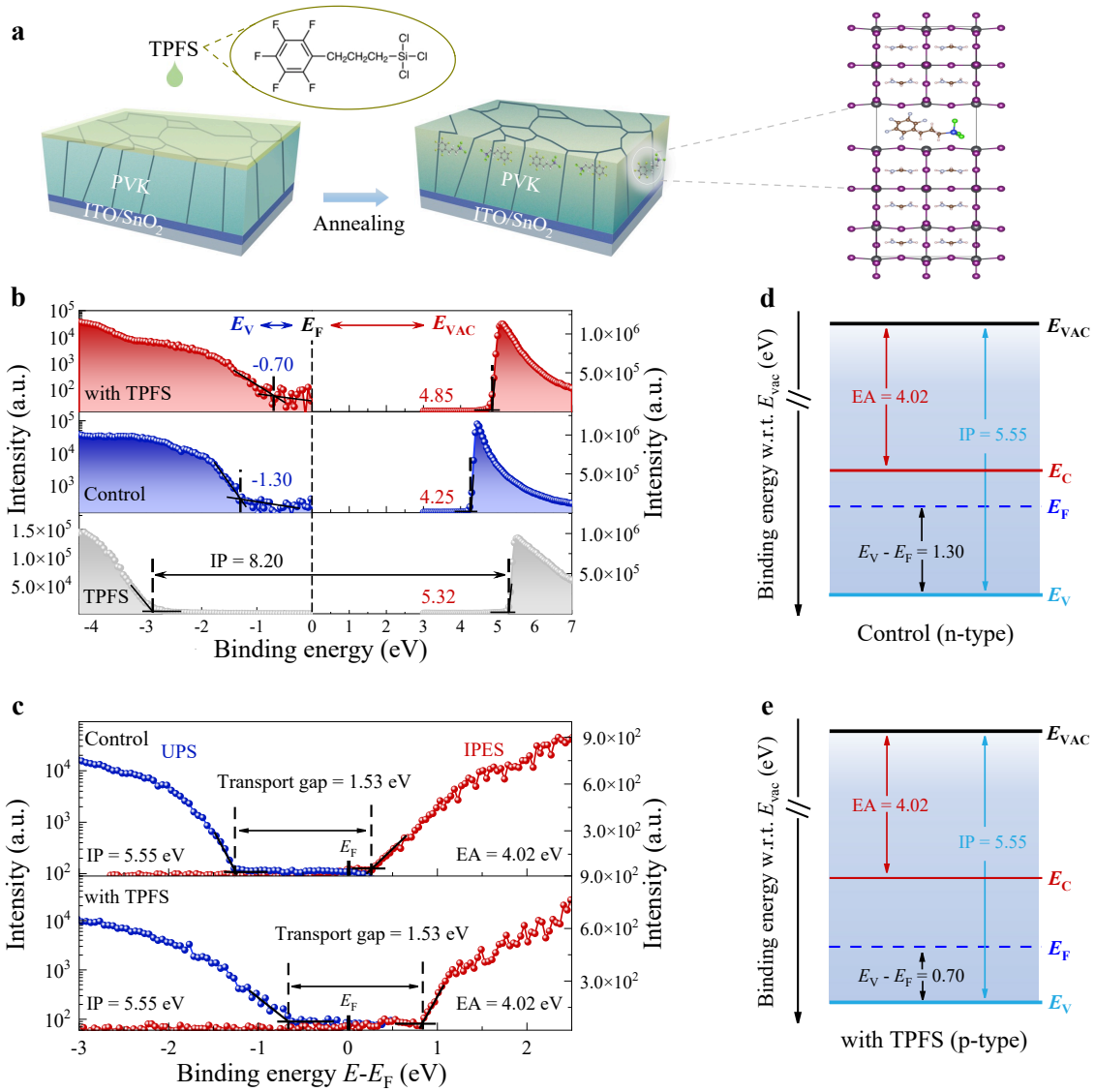

Fig. 1. Perovskite energetics characterizations. (a) Schematic illustration of TPFS surface treatment process. The insets are the molecular structure of TPFS and calculated diffusion of TPFS into perovskites, respectively. **(b)** UPS spectra of secondary electron cutoff region and valence band region of control and TPFS-treated perovskite films. **(c)** IPES spectra. Energy level diagrams of **(d)** control and **(e)** TPFS-treated perovskites.

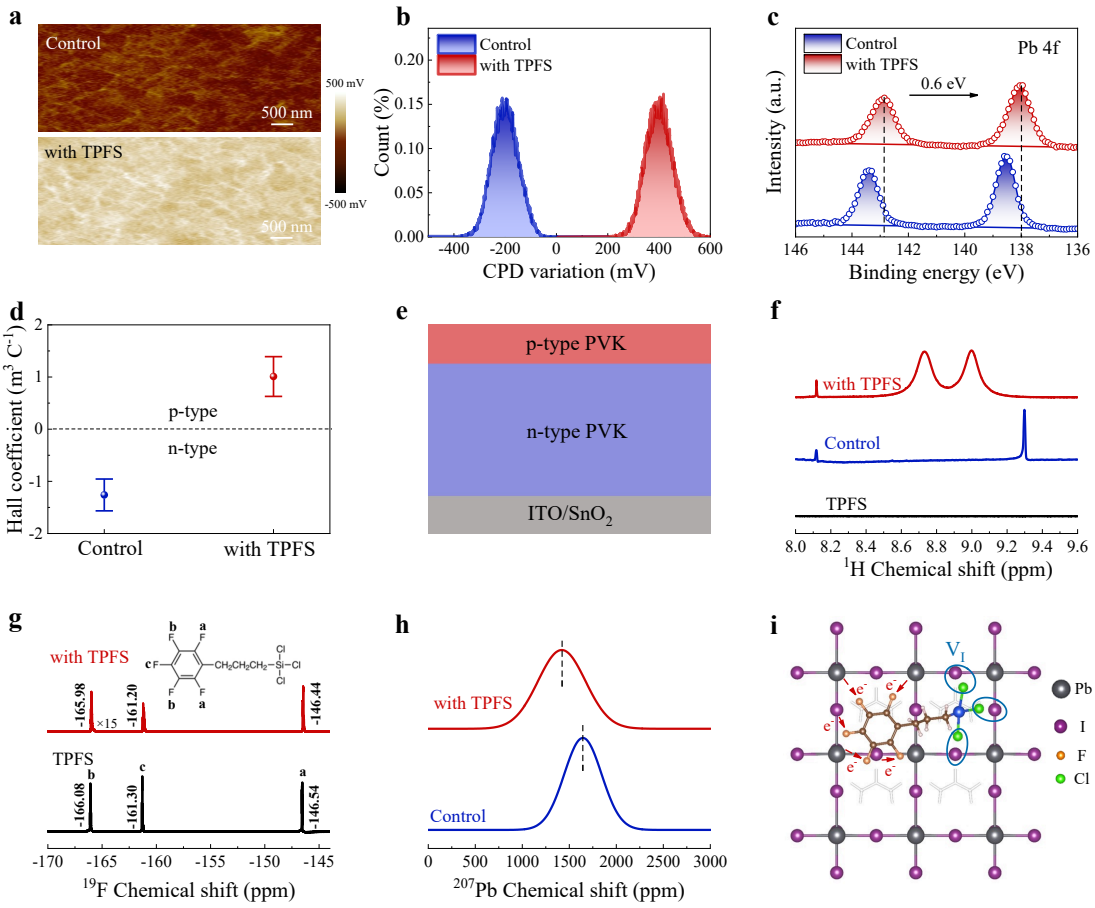

Fig. 2. Impacts of TPFS on surface potential and defect passivation. **(a)** Surface potential images of control and TPFS-treated perovskites from KPFM. **(b)** Statistical potential distributions of film surfaces. **(c)** XPS Pb 4f core level spectra. **(d)** Hall coefficient of perovskite films. **(e)** Schematic illustration of TFPS-treated perovskite film. The thicknesses of n-type and p-type perovskite (labeled as PVK in the figure) are 600 and 100 nm, respectively. **(f)** ^{1}H NMR spectra of TPFS, perovskite and TPFS-treated perovskite. **(g)** ^{19}F NMR spectra. **(h)** ^{207}Pb NMR spectra. **(i)** Theoretical interaction between perovskite and TPFS including Pb-Cl coordination and electron transfer from perovskite to F of TPFS.

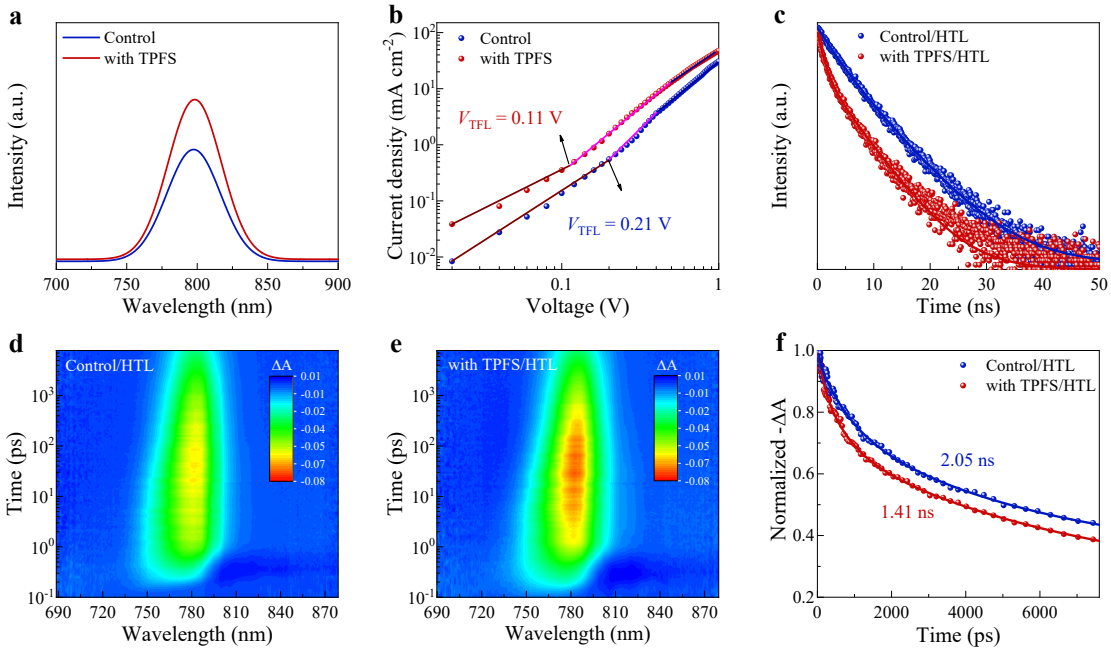

Fig. 3. Interfacial carrier dynamics. (a) PL spectra of control and TPFS-treated perovskite films. **(b)** SCLC curves of hole-only devices. **(c)** TRPL decay curves of control and TPFS-treated perovskite films with HTLs. Ultrafast TAS results of **(d)** control and **(e)** TPFS-treated perovskites with HTLs. **(f)** GSB decay curves of control and TPFS-treated perovskites with HTLs.

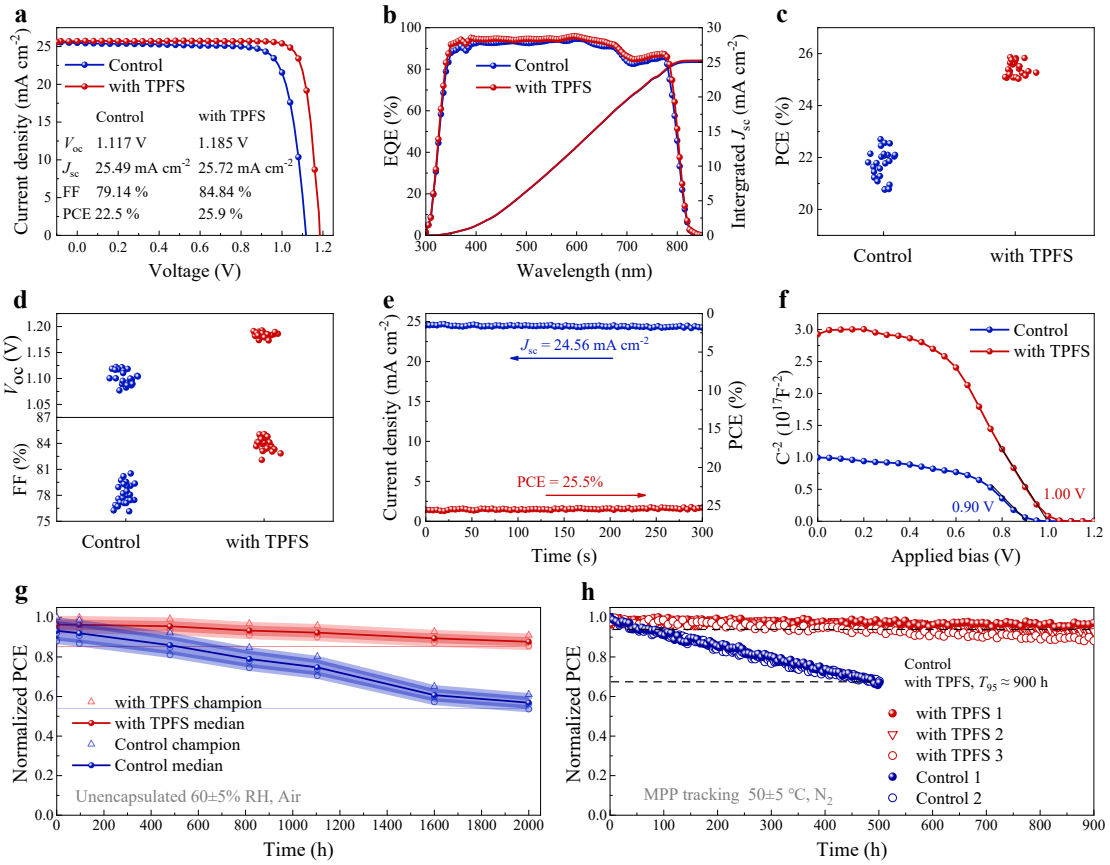

Fig. 4. Photovoltaic performance of PSCs. (a) *J-V* curves of control and TPFS-treated devices. **(b)** EQE spectra and integrated photocurrent densities. **(c)** Statistics of PCE and **(d)** V_{oc} and FF of control and TPFS-treated devices. **(e)** Stabilized power output at MPP of TPFS-treated devices. **(f)** Mott-Schottky plots of control and TPFS-treated devices. **(g)** Operational Stability of control and TPFS-treated devices aged at 60±5% RH in ambient condition. The colored area denotes the standard deviations of devices performance. **(h)** MPP tracking of devices aged under one sun simulated illumination (xenon lamp) at 50±5 °C in N_2 condition.

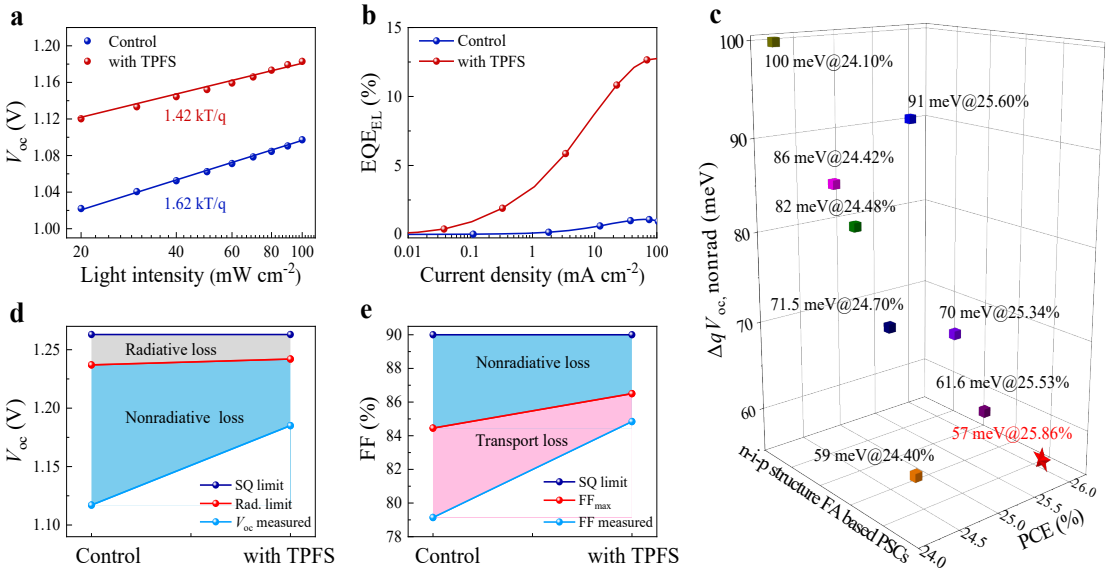

Fig. 5. Nonradiative recombination working principle. (a) Dependence of V_{oc} on light intensity of control and TPFS-treated devices. **(b)** EQE_{EL}-Current density curves of devices operating as LEDs. **(c)** Reported $\Delta qV_{oc,\ nonrad}$ of n-i-p structure FA based PSCs with PCE over 24%. **(d-e)** V_{oc} and FF loss analysis of devices.